



Cite this: *Mater. Adv.*, 2025,
6, 1330

Optimization of photodegradation of crystal violet dye and biomedical applications of greenly synthesized NiO nanoparticles†

Abu Bakar Siddique, ^a Muhammad Ashraf Shaheen, ^{ab} Shakra Shafeeq, Azhar Abbas, ^{ad} Yasir Zaman, ^e Muhammad Zahid Ishaque ^e and Muhammad Aslam ^f

Metal oxide nanoparticles (NPs) are considered suitable candidates for photocatalytic applications because of their large surface area, easy generation of electron–hole pairs for redox reactions and tunable optical properties. Additionally, the successful capping of NP surfaces by bioactive species of plant extracts can further improve their size, shape and bandgap. Inspired by the green synthesis approach, the first time synthesis of nickel oxide NPs (CMFE@NiO NPs) using an aqueous extract of *C. macrocarpa* fruit (natal plum) is reported herein for the photodegradation of crystal violet (CV) dye. The synthesized NPs were characterized by PXRD, UV-vis spectra, FTIR, HR-TEM, EDX, DLS, ZP and TGA. After characterization, CMFE@NiO NPs were evaluated for the degradation of CV dye under sunlight for 120 min. The effect of various reaction parameters, such as pH, temperature, catalyst dose and initial dye concentration, were studied, and reaction conditions were optimized by applying mathematical and statistical tools, *i.e.*, RSM/BBD design. Maximum degradation (99%) of 10 ppm CV solution was observed at a catalyst dose of 50 mg, 358 K and pH 7 with a rate constant value of $3.81 \times 10^{-2} \text{ min}^{-1}$. The effect of radical scavengers was studied to determine major ROS involved and propose a reaction mechanism. Moreover, the antibacterial activity of the NPs was evaluated against Gram-positive and Gram-negative strains. CMFE@NiO NPs showed good inhibition of all bacterial strains with inhibition diameters of $15 \pm 1.5 \text{ mm}$, $14 \pm 1.2 \text{ mm}$, $22 \pm 2.0 \text{ mm}$ and $24 \pm 2.2 \text{ mm}$ for *S. aureus*, *B. subtilis*, *E. coli* and *P. multocida*, respectively. CMFE@NiO NPs were found to be more noxious against Gram-negative bacterial strains. The antioxidant potential of CMFE@NiO NPs also showed good reduction potential to reduce DPPH[•] with an IC_{50} value of $32.9 \pm 2.4 \mu\text{g mL}^{-1}$, which is better than that of the extract ($IC_{50} = 39.3 \pm 2.1 \mu\text{g mL}^{-1}$).

Received 25th October 2024,
Accepted 31st December 2024

DOI: 10.1039/d4ma01078g

rsc.li/materials-advances

1. Introduction

Water pollution caused by azo dyes presents a significant environmental challenge that necessitates effective remediation strategies.¹ Azo dyes are synthetic organic compounds characterized by the presence of one or more azo ($-\text{N}=\text{N}-$)

groups. They are widely used in various industries, particularly textiles, plastics, and food, owing to their vibrant colors and stability. However, their extensive use has led to significant environmental challenges, particularly water pollution. By employing a combination of physical, chemical, and biological methods, it is possible to address the impacts of azo dyes and restore water quality. Continued research on novel materials and techniques, such as advanced nanomaterials and biotechnological approaches, holds promise for enhancing the efficiency and sustainability of azo dye remediation efforts.²

Nickel oxide (NiO) NPs have emerged as a focal point in nanotechnology owing to their distinctive electronic and optical properties. As a transition metal oxide, NiO NPs exhibit a wide range of applications, particularly in areas such as catalysis, sensors, and energy storage.^{3,4} One of the most intriguing aspects of NiO NPs is their energy band gap, which plays a crucial role in determining their optical behavior and functionality. The energy band gap of NiO is typically in the range of

^a Institute of Chemistry, University of Sargodha, Sargodha 40100, Pakistan.

E-mail: ashraf.shaheen@uos.edu.pk

^b Department of Allied Health Sciences, Superior University Lahore (Sargodha Campus), 40100 Sargodha, Pakistan

^c Department of Chemistry, University of Lahore, Sargodha Campus, Sargodha, 40100, Pakistan

^d Department of Chemistry, Government Ambala Muslim College, Sargodha 40100, Pakistan

^e Department of Physics, University of Sargodha, Sargodha 40100, Pakistan

^f Institute of Physics and Technology, Ural Federal University, Mira Str. 19, 620002 Yekaterinburg, Russia

† Electronic supplementary information (ESI) available. See DOI: <https://doi.org/10.1039/d4ma01078g>



3.6–4.0 eV depending on factors such as particle size, synthesis method, and environmental conditions. This wide energy band gap allows NiO NPs to exhibit semiconducting behavior, making them particularly suitable for applications in photocatalysis and solar energy conversion. The ability to absorb UV-visible light and facilitate charge carrier generation is a key feature that enhances its effectiveness in various photocatalytic processes, including the degradation of organic pollutants, such as azo dyes.^{3,5}

The sensitivity of NiO NPs to changes in their surroundings, coupled with their tunable optical properties, makes them promising candidates for developing innovative photocatalysts.⁶ The surface modification of NiO NPs can be achieved by applying a green synthesis approach. It has been previously reported that greenly synthesized NiO NPs have diverse functional groups on their surface, highly stable, and tunable optical properties, *i.e.*, energy bandgap. The phyto-functionalized NPs can serve as excellent photocatalysts for azo dye degradation by optimizing the reaction conditions.⁷ Owing to the miraculous advantages of green synthesis, various plant materials have been utilized to synthesize NPs, but the bioactive enriched *C. macrocarpa* fruit aqueous extract has never been used to synthesize NiO NPs.

C. macrocarpa belongs to one of the largest plant families, *i.e.*, the Apocynaceae family. It is an evergreen shrub, also called natal plum, which is commonly found in the subtropical and tropical regions of Asia and Africa.⁸ Its ripened fruits, leaves and stems are enriched in various bioactives, such as alkaloids, flavonoids, saponins, triterpenoids, steroids, quinones, tannins, carbohydrates and phenols. The natal plum contains a considerable number of phytochemicals, such as phenolics (caffeic acid, catechin, quercetin-3-O-glucoside, coumaroylquinic acid, *etc.*), flavonoids, alkaloids, terpenoids, saponins, vitamins and minerals.^{8–10} Natal plum is commonly used in desserts, sauces, ice cream, jellies and jams. It is also used in traditional medicines to cure cough and diarrhea in livestock and to cure various microbial diseases.¹⁰ Owing to its phytochemical enriched nature, it can be hypothesized that the *C. macrocarpa* fruit aqueous extract can mediate the synthesis of NiO NPs with improved optical, catalytic and biological properties.

Response surface methodology (RSM) is a statistical and mathematical technique used to optimize processes and improve product quality. It is particularly useful when several variables influence a response variable, allowing researchers to analyze the interactions between these factors effectively.¹¹ RSM employs various designs, among which the Box–Behnken design is one of the most popular because of its efficiency and practicality in exploring quadratic response surfaces. The Box–Behnken design is a specific type of RSM involving a three-level factorial design. It requires fewer experiments than full factorial designs and provides adequate information to model the complex relationships between variables. The effect of temperature, azo dye concentration, catalyst dose and pH of reaction can be optimized by applying the RSM/BBD model to obtain highly efficient results of photodegradation reactions.¹²

Nickel oxide (NiO) NPs have attracted considerable interest in recent years owing to their remarkable antibacterial and antioxidant properties. These characteristics not only highlight

their potential in various applications, including biomedical and environmental fields but also contribute to addressing pressing health concerns related to microbial resistance and oxidative stress.¹³ NiO NPs exhibit effective antibacterial activity against a range of Gram-positive and Gram-negative bacteria. The primary mechanisms by which these nanoparticles exert their antibacterial effects include the generation of reactive oxygen species (ROS), disruption of bacterial membranes, and interference with cellular processes. Upon contact with bacteria, NiO nanoparticles can induce oxidative stress by generating ROS, leading to cellular damage, including lipid peroxidation and DNA fragmentation. This oxidative damage disrupts essential metabolic functions and ultimately results in bacterial cell death.¹⁴ Moreover, NiO NPs have also demonstrated significant antioxidant activity by scavenging free radicals and reducing oxidative stress. Their ability to donate electrons allows them to neutralize free radicals, thereby preventing cellular damage and maintaining the redox balance within biological systems.¹⁵

In the present study, NiO NPs are greenly synthesized using a bioactive-enriched aqueous extract of *C. macrocarpa* to degrade CV dye. These NPs are characterized by UV-visible spectroscopy, FTIR, PXRD, EDX, HR-TEM, DLS, ZP and TGA analyses. After successful characterization, the CMFE@NiO NPs are evaluated for their photocatalytic potential to degrade CV dyes under sunlight. The effects of various reaction conditions on the photodegradation capability of the catalysts were assessed, and the conditions were optimized using the RSM/BBD model. The effect of radical scavengers was studied to determine the major ROS involved in the reaction and to propose a degradation mechanism. CMFE@NiO NPs are also evaluated for antibacterial applications against Gram-positive and Gram-negative strains by a standard disc diffusion assay and for antioxidant potential by DPPH assay.

2. Experimental work

2.1. Materials and instruments used

High purity chemicals purchased from Sigma Aldrich and Merck, Germany, were used for experimental work. All the solutions were prepared in double-deionized water. Chromic acid solution was used to wash the glassware, followed by drying the glassware in an oven. *C. macrocarpa* fruit was collected from the plant nursery of the University of Sargodha, Pakistan.

Powder X-ray diffraction (PXRD) spectra were recorded on a JDX-3532 X-ray diffraction (XRD) instrument from JEOL, Japan. Functional group analysis was performed by recording FTIR spectra using the Shimadzu FTIR-8400S spectrophotometer (Japan), and absorbance spectra were obtained using the Shimadzu UV-1800 spectrophotometer (Japan). High-resolution transmission electron microscopy (HRTEM) analysis was performed using a JEM-ARM2000F instrument from JEOL, Japan. TGA graphs were obtained using a Discovery 650 SDT thermal analyzer (TA Instruments, USA) in the temperature range of 25–1000 °C. Mineralization of the dye was determined based on total organic carbon content measurements (TOC) using a total

organic carbon analyzer, TOC-V_{CPN}, Shimadzu, Japan, before and after the photocatalysis of the CV dye.

2.2. Preparation of CMFE

Aqueous extract of *C. macrocarpa* fruit (CMFE) was synthesized following the procedure reported earlier.¹⁶ The procedure involved washing, slicing, drying and grinding of natal plum. The powder obtained (10 g) was refluxed in DW (100 mL) at 90 °C for 3 h. The resulting liquid enriched with phytochemicals was filtered to discard the solid waste. Filtrate was evaporated in the oven (80 °C, 24 h), and powder (CMFE) was kept in a dried petri dish to synthesize NPs.

2.3. Green synthesis of NiO NPs

To synthesize CMFE@NiO NPs, separate aqueous solutions of Ni(NO₃)₂·6H₂O (30 mM, 20 mL) and CMFE (20 mg, 15 mL) were prepared in deionized water. Aqueous extract and salt solution were mixed at a constant stirring rate of 200 rpm and pH 9 for 30 min, followed by the addition of 10 mL of 0.1 M NaOH to adjust pH 9. Subsequently, the resulting mixture was stirred (200 rpm) for 30 min at 100 °C. The appearance of dark green precipitates indicated the synthesis of Ni(OH)₂ powder. The synthesized powder was isolated from the mixture by centrifugation (8000 rpm, 30 min). The powder was rinsed three times with DW, dried in an oven (75 °C, 4 h), and subjected to calcination (350 °C, 2 h) in a muffle furnace. This thermal treatment was carried out to decompose the Ni(OH)₂ to NiO NPs, and the temperature of 350 °C was selected due to the formation of small size NiO NPs at low temperatures in the range of 300–400 °C, as reported in the literature.¹⁷ The UV-vis spectrum of these CMFE@NiO NPs sonicated in distilled water showed the presence of a characteristic peak at 311 nm.

2.4. Photocatalytic degradation of CV

The photodegradation of CV was conducted on the surface of CMFE@NiO NPs under direct sunlight according to the described methodology.¹⁸ The solution of CV (10 ppm, 20 mL) was mixed with the specified quantity of CMFE@NiO NPs, and the resultant mixture was agitated in the dark for 20 min to establish adsorption–desorption equilibria on the surface of the CMFE@NiO NPs. Subsequently, the mixture was subjected to sunlight for 120 min, and the reduction in the solution's absorbance was recorded at 15-minute intervals. The mixture of the catalyst and dye solution was placed in a covered glass chamber and exposed directly to sunlight to avoid any exposure to humidity. Additionally, these experiments were carried out in the daytime (12:00–13:30 pm) on August 24, 2024 at 35 ± 2 °C. When performing each set of experiments, the same conditions were maintained. The progressive reduction in the characteristic absorbance of the solution ($\lambda_{\text{max}} = 599$ nm) unequivocally signified the degradation of the CV dye. The percentage degradation of the solution was determined using eqn (1):^{19,20}

$$\% \text{Degradation of CV} = \frac{C_0 - C_f}{C_0} \times 100 = \frac{A_0 - A_f}{A_0} \times 100 \quad (1)$$

where C_0 and C_f denote the starting and final concentrations of the dye, respectively. The influence of various process parameters on degradation kinetics was examined. The factors encompass pH, catalyst dosage, initial concentration of CV, and temperature. The response surface approach, particularly the Box–Behnken design, was utilized to optimize these parameters.

2.5. Experimental design of RSM/BBD

For comparison of empirical models with experimental findings, RSM is a beneficial statistical and mathematical tool that provides access to the interactions of different reaction parameters on the degradation of dye.^{21,22} The Box–Behnken design (BBD) methodology was employed to establish the experimental protocols under defined reaction conditions. The influence of temperature, pH, catalyst dosage, and initial concentration of CV on the photodegradation process was examined. As shown in Table S1 (ESI†), these variables were analyzed at two levels: low (−1) and high (+1). To validate the BBD, 29 experimental runs for CV decomposition for four factors were conducted, and the outcomes were compared with the predicted values.

2.6. Total organic content (TOC) analysis

If azo dyes are not completely broken down, additional dangerous species might be produced that may further deteriorate water quality.²² The only indication for the color removal of the solution is not sufficient to achieve complete degradation. The breakdown of the diazenyl functional group of azo compounds causes the color to disappear, while mineralization is the whole conversion of compounds and intermediate species to carbon dioxide and water.²³ Consequently, it is essential to estimate the TOC value at regular intervals to analyze the mineralization of CV. %Removal of TOC was calculated using eqn (2):²⁴

$$\% \text{Removal of TOC (mineralization)} = \frac{(\text{TOC}_0 - \text{TOC}_t)}{\text{TOC}_0} \times 100 \quad (2)$$

where TOC₀ and TOC_t represent the initial concentration of organic content and the concentration of organic content after time 't', respectively.

2.7. Reusability studies of catalysts

A reusability study was carried out over five consecutive cycles to evaluate the capability of CMFE@NiO NPs for the degradation of CV. Following each batch experiment, the CMFE@NiO NPs were regenerated by employing the method described in the literature.²⁵ Upon the end of each cycle, the catalyst was extracted from the mixture *via* centrifugation (3000 rpm, 10 min). The catalyst was cleaned with DW after removing the upper liquid layer and subsequently activated by drying in an oven at (80 °C, 4 h). The CMFE@NiO NPs were effectively utilized for the subsequent cycle. After 5th cycle of use, the CMFE@NiO NPs were characterized by PXRD and FTIR analysis to access the physicochemical properties of NPs.

2.8. Disc diffusion assay

The bactericidal efficacy of CMFE and CMFE@NiO NPs was assessed utilizing the conventional disc diffusion method.²⁶ Four bacterial colonies, specifically two Gram-negative strains (*E. coli* and *P. multocida*) and two Gram-positive strains (*S. aureus* and *B. subtilis*), were cultured in a nutritional agar solution (2.5 g/100 mL) for 24 h at 4 °C. The turbidity of the bacterial colonies was set to 108 CFU. Following autoclaving, sterilized paper discs containing 1 mL of CMFE (2 mg/5 mL), CMFE@NiO NPs (2 mg/5 mL) and rifampicin (2 mg/5 mL) were arranged on Petri dishes. After incubation of Petri dishes (24 h, 37 °C), the zone of inhibition for each sample was measured in millimeters. The zones of inhibition of the samples were compared with the rifampicin used as a positive control.

2.9. DPPH (2,2-diphenyl-1-picryl-hydrazyl-hydrate) assay

The antioxidant potential of CMFE@NiO NPs was assessed using a DPPH assay, which involved hydrogen donation or radical scavenging of DPPH radical.²⁷ The DPPH radical was scavenged, and a pale-yellow solution appeared due to the stable DPPH molecule. In summary, a 0.1 mM solution of DPPH radical was prepared and stored in the dark for 2 h. The CMFE, NPs, and gallic acid solutions (1 mg mL⁻¹) were prepared in methanol and diluted to prepare multiple aliquots in the range of 12.5–400 µg mL⁻¹. 800 µL of each dilution was mixed with 1.2 mL of DPPH[•] solution in a test tube. After immediate mixing for 10 s, each test tube was placed in the dark at room temperature for 30 min. After 30 min, the absorbance of each solution was measured at 517 nm. The %DPPH radical scavenging (inhibition) and IC₅₀ value were determined using eqn (3) and (4), respectively:

$$\% \text{DPPH radical scavenging} = \frac{(A_0 - A_s)}{A_0} \times 100 \quad (3)$$

$$\text{IC}_{50} = \frac{(50 - \text{intercept})}{\text{slope}} \times 100 \quad (4)$$

where A_0 and A_s represent the absorbance of the blank and sample solutions, respectively.

2.10. Statistical analysis

Each experiment was analyzed three times to assess its statistical significance using ANOVA. At a threshold of $p < 0.05$, statistical significance was acknowledged. The mean \pm standard deviation was used to report all of the data.

3. Results and discussion

3.1. UV-vis and FTIR analyses

The UV-vis absorbance spectrum was recorded to identify the synthesis of NiO NPs and the energy bandgap (E_g) between the valence band (VB) and the conduction band (CB) by observing the characteristic peak and absorbance values. The sonicated sample of NPs (Fig. 1(a)) showed a characteristic peak of NiO NPs at 311 nm, attributed to surface plasmon resonance.²⁸ Tauc plot (inset of Fig. 1(a)) between energy (eV) and $(\alpha h\nu)^2$ showed an E_g value of 3.18 eV. These band gap calculations are provided in ESI,† Section S1. The optical band gap of CMFE@NiO NPs reported in the current study is similar to the band gap reported in the literature. For example, the optical band gap of 2.88 eV was estimated for NiO NPs synthesized using polyvinylpyrrolidone (PVP) as a surfactant.²⁹ In another study, the band gap energies of NiO NPs were found to be 3.44, 3.38, 3.25, and 2.86 eV at 300, 400, 500, and 600 °C, respectively.¹⁷ The optical band gaps of NiO NPs derived from four different organic precursors were also found to be 2.45, 2.82, 2.93, and 3.12 eV.³⁰ This value of band gap also showed the sunlight/visible light responsiveness of NPs for charge transfer phenomenon in the lattice and generation of charge carriers in VB and CB.

The FTIR spectra of CMFE and CMFE@NiO NPs were examined to determine the predominant functional groups present in the samples. Fig. 1(b) presents the comparative FTIR spectra of CMFE and CMFE@NiO NPs. The CMFE spectrum indicated the presence of many functional groups derived from the diverse bioactive compounds in the extract, including phenolics, alkaloids, and flavonoids. The principal absorbance peaks identified at around 1450 cm⁻¹, 1700 cm⁻¹, 2300 cm⁻¹, 2900 cm⁻¹, and 3250–3600 cm⁻¹ were attributed to the

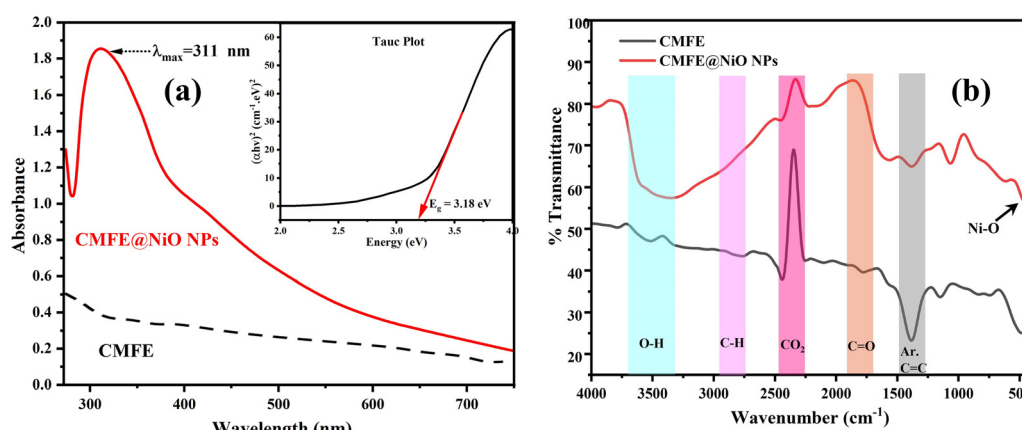


Fig. 1 (a) UV-vis spectra of CMFE and CMFE@NiO NPs and Tauc plot of CMFE@NiO (inset). (b) FTIR spectra of CMFE and CMFE@NiO NPs.



aromatic rings ($C=C$), carbonyl groups ($C=O$), atmospheric CO_2 , alkyl groups ($C-H$), and hydroxyl groups ($O-H$) stretching's present in the CMFE samples, respectively.²⁷ The attribution of peaks between $2300-2400\text{ cm}^{-1}$ is due to atmospheric CO_2 .³¹ Additionally, the CMFE@NiO NP spectra displayed these peaks, including a peak of about 510 cm^{-1} associated with the Ni–O bonds.¹⁷ Although finger print region in the FT-IR spectra is not much reliable, many peers have reported that metal–oxygen bonds are absorbed in the range of $400-700\text{ cm}^{-1}$.^{17,32} The detection of hydroxyl, carbonyl, and aromatic ring peaks in the CMFE@NiO NP spectrum indicated the effective capping of NiO NPs by bioactive species.

3.2. XRD, HR-TEM and EDX analyses

The PXRD spectrum of CMFE@NiO NPs is illustrated in Fig. 2(a) in the 2θ range of $20-80^\circ$. According to JCPDS file no. 04-0835, Bragg's reflections observed at 2θ values of 37.4° , 43.3° , 62.9° , 75.5° and 79.5° were assigned to crystal planes (111), (200), (220), (311) and (222), respectively. These strong Bragg's reflections correspond to diffraction lattice planes, confirming the face-centered cubic crystal structure of CMFE@-NiO NPs with space group $Fm\bar{3}m$. The Debye–Schererrer relation (eqn (5)), dislocation density (δ) formula (eqn (6)), micro strain (ε) formula (eqn (7)) and degree of crystallinity (eqn (8)) were used to compute the crystal parameters, which include crystallite size, dislocation density, micro strain and degree of crystallinity, respectively, as depicted in Table 1.

$$D = \frac{k\lambda}{\beta \cos \theta} \quad (5)$$

$$\delta = \frac{1}{D^2} \quad (6)$$

$$\varepsilon = \frac{\beta}{4 \tan \theta} \quad (7)$$

$$\text{Degree of crystallinity} = \frac{\text{Area of crystalline peaks}}{\text{Area of all peaks}} \times 100 \quad (8)$$

where the average crystallite size, Scherer constant, X-ray wavelength, diffraction angle, and peak FWHM are represented by D , K , λ , θ , and β , respectively. Using non-linear fitting to the XRD pattern, FWHM values were calculated at 2θ values, and the average crystallite size was calculated to be 9.8 nm . All the relevant calculations are provided in Section S2 of the ESI.†

Analysis of the structural and elemental composition of the CMFE@NiO NPs was conducted using HR-TEM and EDX,

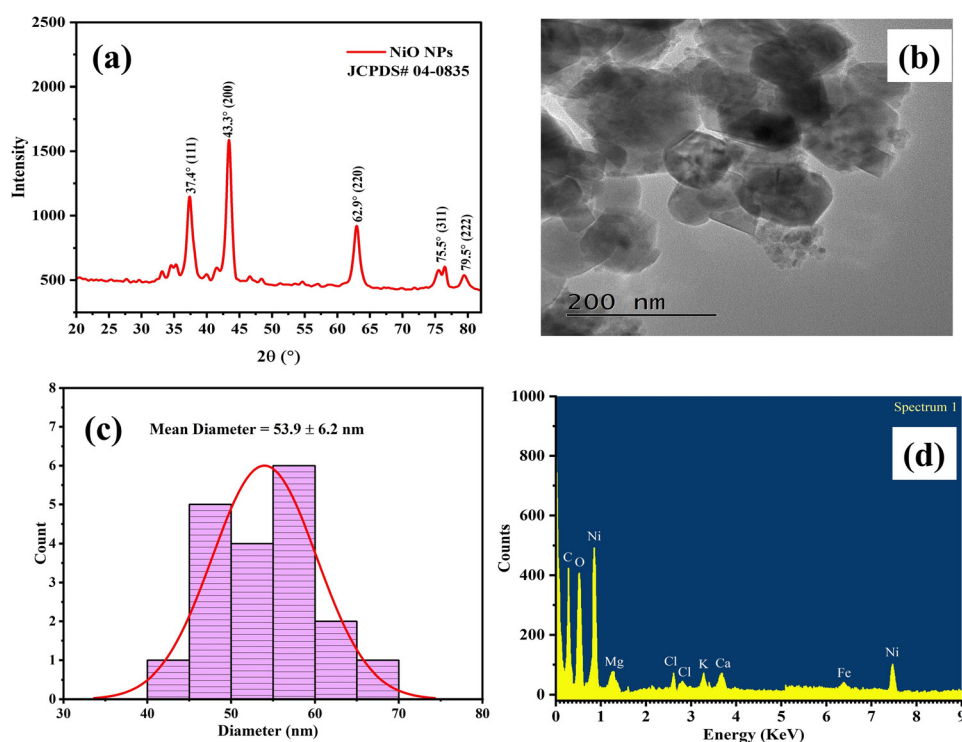


Fig. 2 (a) PXRD spectrum of CMFE@NiO NPs; (b) HR-TEM image of CMFE@NiO NPs; (c) histogram of the particle size of CMFE@NiO NPs and (d) EDX analysis of CMFE@NiO NPs.

Table 1 Crystal parameters of CMFE@NiO NPs

Sample	Average crystallite size 'D' (nm)	Dislocation density $\delta \times 10^{-3}$ (nm^{-2})	Micro strain $\varepsilon \times 10^{-3}$	Degree of crystallinity (%)
CMFE@NiO NPs	9.8	10.2	1.7	95.1



respectively. An HR-TEM image of the CMFE@NiO NPs was obtained to examine the morphology and dimensions of the particles, as shown in Fig. 2(b). The TEM picture (Fig. 2(b)) indicated the presence of quasi spherical-shaped NPs. Analysis of the TEM image was conducted to determine the distribution of particle sizes and the average particle size, as depicted in the histogram in Fig. 2(b) and (c). The mean particle size of CMFE@NiO NPs was determined to be 53.9 ± 6.2 nm (Fig. 2(c)). Furthermore, the EDX spectra (Fig. 2(d)) of CMFE@NiO NPs exhibited prominent $L\alpha$ and $K\alpha$ peaks of Ni at 0.85 and 7.47 keV, respectively, and $L\alpha$ lines of oxygen at 0.52 keV. In addition to these peaks, other peaks of different elements, including C, Zn, Al, Na, Cl and Si, were also observed due to the various bioactive compounds in the capping agent on the surface of CMFE@NiO NPs. These additional peaks are generally observed in the greenly synthesized NPs.¹⁴

3.3. Hydrodynamic diameter and stability of CMFE@NiO NPs

The greenly synthesized NPs have a cloud of water molecules attached to their surface in the aqueous media that provides them with colloidal stability and contributes to the total radius of NPs (hydrodynamic radius). To determine the hydrodynamic radius of the NPs, the DLS analysis was carried out. This test revealed a narrow distribution of particle sizes (80–98 nm) of the NPs, with an average diameter of 87.6 ± 5.1 nm (Fig. 3(a)). This result exhibited strong concordance with the HR-TEM findings.

Based on the ZP analysis, the average ZP value by surface charge determination was found to be -28.9 ± 4.1 mV, as illustrated in Fig. 3(b). This negative value due to the capping of phytochemicals on the surface implies moderate colloidal stability of NPs in the liquid phase. Based on the ZP measurements, the suspension was reported to be electrostatically stable and resistant to agglomeration in aqueous media.

3.4. Thermogravimetric analysis of CMFE@NiO NPs

As shown in Fig. 4, the thermal stability of CMFE@NiO NPs was evaluated using TGA analysis in a temperature range of 25–1000 °C. Fig. S1 (ESI[†]) shows the DTG curves for the CMFE@NiO NPs. The DTG curves were plotted to validate the temperature assignments for each degradation step. The structure and

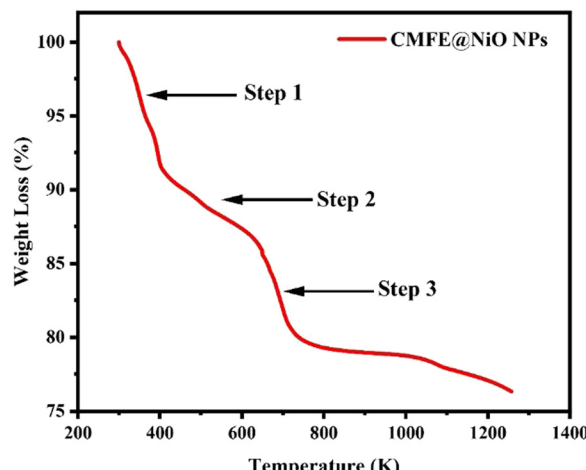


Fig. 4 TGA curve of CMFE@NiO NPs.

disintegration process of CMFE@NiO NPs were found to be highly congruent with the TGA data when the material was heated. There were three separate stages of thermal degradation of CMFE@NiO NPs. Initially, a modest reduction in weight (about 8%) was observed within the temperature range of 301–400 K. This reduction was ascribed to the depletion of water molecules during dehydration and the elimination of moisture from the surface. In the second stage, a 6% reduction in weight was observed within the temperature range of 405–636 K. The observed decrease in weight was attributed to the breakdown of the organic components bound to the surface of the NPs. In the temperature range of 640–735 K, a weight reduction of 7% was observed as a consequence of the disintegration of Ni–O bonds on the surface and the subsequent pyrolysis of CMFE@NiO NPs. In general, the thermal data indicated that the sample exhibited excellent stability, with a little 21% weight loss, even when exposed to temperatures above 1200 K.

3.5. Photodegradation of crystal violet (CV)

Previously, many photocatalysts have been reported to absorb high energy radiations, such as UV rays, for surface activation and charge separation, which results in their catalytic performance (Table S2, ESI[†]), but the high energy requirement is the

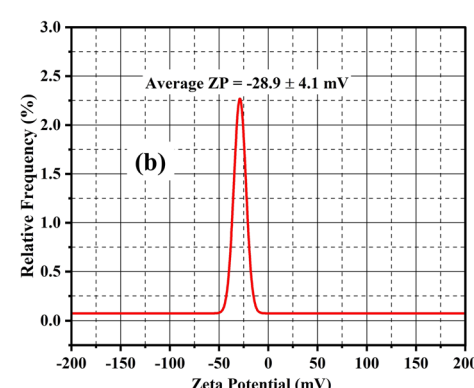
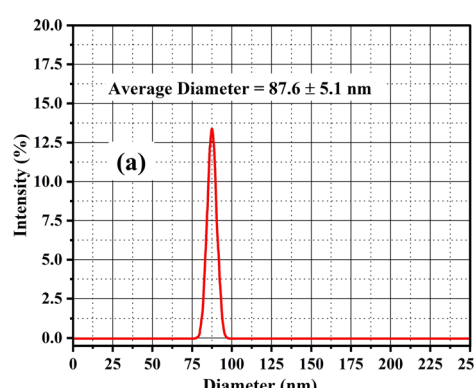


Fig. 3 (a) DLS data and (b) zeta potential analysis of CMFE@NiO NPs.



Table 2 Four factor BBD model with experimental results and predicted values

Run	A: pH	B: temperature (K)	C: concentration of dye (ppm)	D: catalyst dosage (mg)	CV dye degradation (%)	
					Actual value	Predicted value
1	3	328	30	30	57	59.19
2	13	298	20	30	42	43.19
3	8	328	20	30	90.5	90.10
4	13	328	30	30	33	33.27
5	8	298	20	50	93	92.02
6	13	328	20	50	42	41.29
7	8	298	20	10	86	85.27
8	8	358	10	30	91	92.13
9	8	328	20	30	89.5	90.10
10	13	328	20	10	35	36.79
11	8	328	20	30	89	90.10
12	8	328	10	10	89	87.52
13	8	328	30	10	79	78.35
14	3	328	20	50	68.5	65.96
15	8	358	20	10	79	80.10
16	3	358	20	30	61	60.44
17	3	298	20	30	59	60.10
18	8	328	20	30	94	90.10
19	13	358	20	30	39	38.52
20	3	328	20	10	51	50.96
21	8	298	10	30	95	96.29
22	13	328	10	30	51	48.94
23	8	328	10	50	96	97.27
24	3	328	10	30	62	61.85
25	8	358	20	50	92	92.85
26	8	298	30	30	87	85.13
27	8	358	30	30	87	84.96
28	8	328	20	30	87.5	90.10
29	8	328	30	50	86	88.10

Table 3 Fit summary of the model by software for CV degradation

Source	Sequential <i>p</i> -value	Lack of fit <i>p</i> -value	Adjusted <i>R</i> ²	Predicted <i>R</i> ²	Remarks
Linear	0.4600	0.0003	-0.0092	-0.2952	
2FI	0.9999	0.0001	-0.3345	-1.5738	
Quadratic	<0.0001	0.6696	0.9889	0.9762	Suggested
Cubic	0.3981	0.8546	0.9904	0.9747	Aliased

main drawback of these catalysts.^{33,34} Therefore, the development of new nanocatalysts that can easily absorb inexpensive sunlight/visible radiations to perform catalytic applications is highly explored nowadays. Hence, owing to an E_g value of 3.18 eV, the CMFE@NiO NPs were explored for their catalytic applications to degrade hazardous dyes. Photodegradation of CV was carried out on the surface of CMFE@NiO in the presence of sunlight due to an appropriate bandgap (3.18 eV). This bandgap denotes the sunlight harvesting ability of CMFE@NiO for the generation of charge carriers (e^-/h^+ pairs) for redox reaction with dye molecules. The UV-vis spectra of the CV dye solution were recorded at λ_{max} (599 nm) every 15 min for 120 min of sunlight exposure. The decrease in the absorbance showed a gradual decline in the concentration of dye (Fig. S2, ESI†).

3.6. RSM/BBD for optimization of CV degradation

The effect of the four independent variables and their interrelation on CV degradation was studied by applying the RSM/BBD model. The results of 29 runs of experiments suggested

using the BBD model are depicted in Table 2 along with the predicted and actual results obtained. A high degree of agreement between adjusted R^2 (0.9889) and predicted R^2 (0.9762) with a difference of less than 0.2, insignificant lack of fit *p*-value (0.6696), sequential *p*-value (<0.0001) and a standard deviation of 2.22 suggested the quadratic model for CV degradation.^{21,35} For adequate fitting of the model, as far as the lack-of-fit *p*-value (0.6696) is concerned, the *p*-value for the lack-of-fit test must be more than 0.05 ($p > 0.05$). A lack of fit *p*-value greater than the significance level means that the model fits the data well. A fit summary of the model proposed by applying the software is shown in Table 3. The experimental and predicted findings displayed in Fig. S3 (ESI†) exhibited a high level of agreement.

Table 4 displays the results of an analysis of variance (ANOVA) test conducted to determine the model's validity and relevance as suggested by the BBD. A significant model was indicated by a model *F*-value of 179.99.

Model terms were considered statistically significant when their *p*-values were less than 0.05. In this case, it was found that A^2 , D^2 , AC , AD , C , and D were all statistically significant.



Table 4 ANOVA of the quadratic polynomial model for CV degradation

Source	Sum of squares	df	Mean square	F-Value	p-Value	Remarks
Model	12 398.87	14	885.63	179.99	<0.0001	Significant
<i>A</i> -pH	1131.02	1	1131.02	229.86	<0.0001	
<i>B</i> -temperature	14.08	1	14.08	2.86	0.1128	
<i>C</i> -concentration of dye	252.08	1	252.08	51.23	<0.0001	
<i>D</i> -catalyst dosage	285.19	1	285.19	57.96	<0.0001	
<i>AB</i>	6.25	1	6.25	1.27	0.2787	
<i>AC</i>	42.25	1	42.25	8.59	0.0110	
<i>AD</i>	27.56	1	27.56	5.60	0.0329	
<i>BC</i>	4.00	1	4.00	0.8129	0.3825	
<i>BD</i>	9.00	1	9.00	1.83	0.1977	
<i>CD</i>	0.0000	1	0.0000	0.0000	1.0000	
<i>A</i> ²	9954.69	1	9954.69	2023.09	<0.0001	
<i>B</i> ²	0.8524	1	0.8524	0.1732	0.6836	
<i>C</i> ²	0.0821	1	0.0821	0.0167	0.8991	
<i>D</i> ²	30.69	1	30.69	6.24	0.0256	
Residual	68.89	14	4.92			
Lack of fit	45.19	10	4.52	0.7627	0.6696	Not significant
Pure error	23.70	4	5.93			
Total	12 467.76	28				

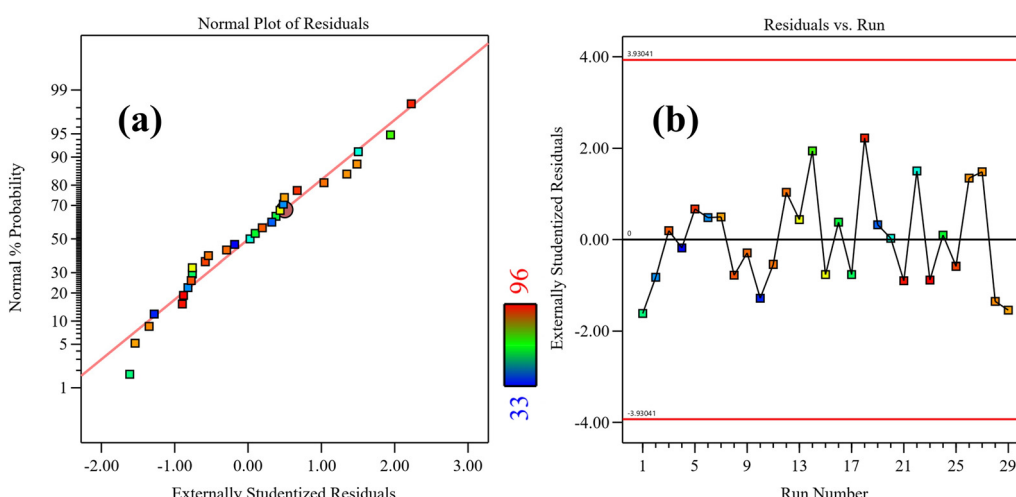


Fig. 5 (a) Normal plot of residuals and (b) residual vs. run distribution.

The *F*-value of 0.76 for the lack of fit showed that the lack of fit was insignificant compared to the pure error. For a given value for each parameter, the equation stated in terms of the coded factors can be used to anticipate the response. The ultimate equation (eqn (9)) expressing the coded factors for the deterioration of CV becomes

$$\begin{aligned} \text{CV degradation (\%)} = & 90.10 - 9.71A - 1.08B - 4.58C + 4.88D \\ & - 1.25AB - 3.25AC - 2.62AD + BC + 1.5BD - 39.17A^2 \\ & - 0.3625B^2 - 0.1125C^2 - 2.17D^2 \quad (9) \end{aligned}$$

where the intercept is 90.10; the coefficients of *A*, *B*, and *C* represent the slopes or regression coefficients for the linear effects; *A*², *B*², *C*², and *D*² represent the quadratic effects; and *AB*, *AC*, *AD*, *BC*, *BD*, and *CD* represent the regression coefficients for the 2-factor interaction effects. This equation enables predictions of the response at specified levels of each parameter.

Moreover, Fig. S3 (ESI†) provides evidence of a substantial degree of agreement between the experimental and predicted results.

Furthermore, the normal plot of residuals (Fig. 5(a)) and residual vs. run plots (Fig. 5(b)) were analyzed to check the suitability of the model. The linearity of the normal plot of residuals and the random rise and fall of residuals of each run around the central line indicate the appropriate fit of the model.

Two-dimensional contour plots and three-dimensional response surface graphs are used to assess the concurrent impact of two variables on the efficiency of dye degradation within specified ranges while keeping the other variables constant. Fig. 6 displays 2-D contour plots and 3-D response surface visualizations for different parameters.

Based on Fig. 6(a), it is evident that the degradation efficiency increases as the temperature increases at pH 8. An optimal



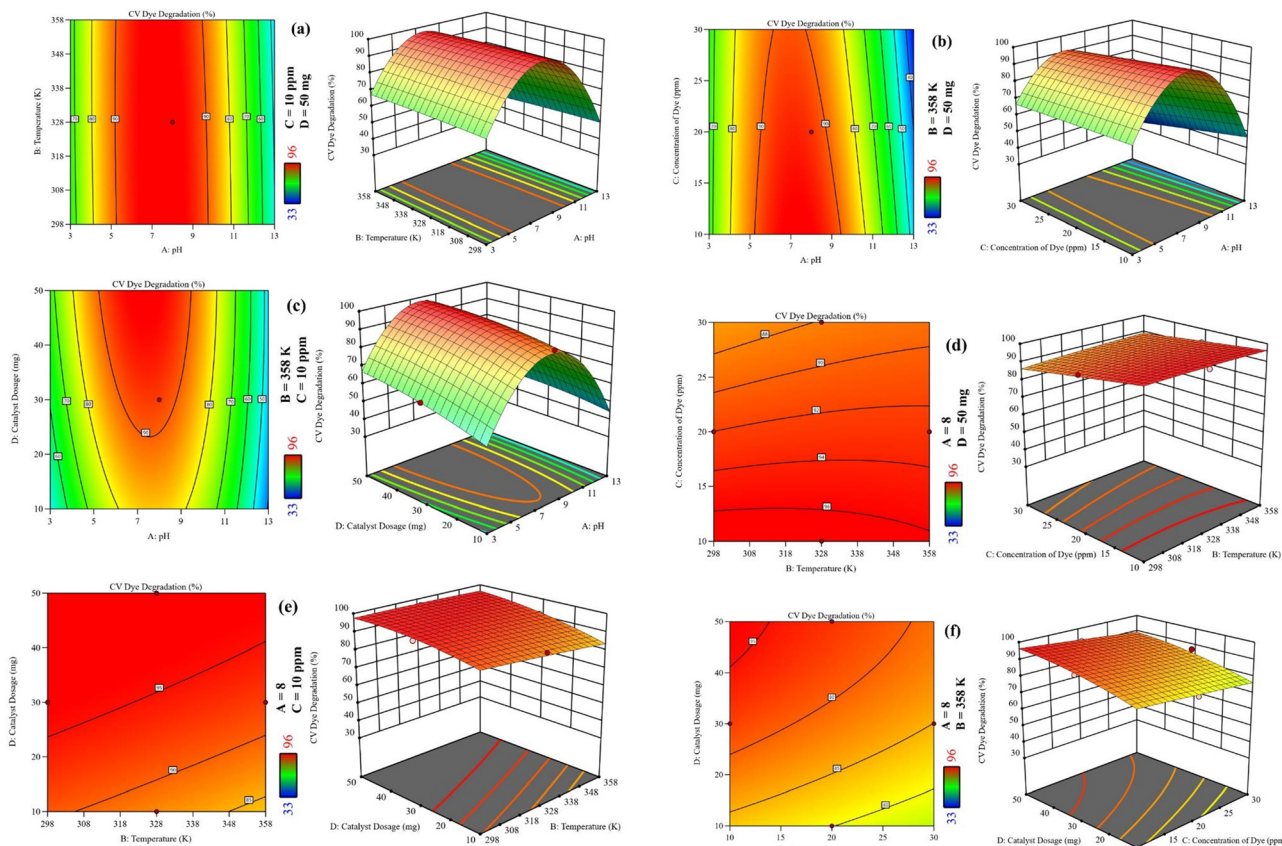


Fig. 6 2-D contour plots and 3-D response surface graphs of interaction of (a) pH and temperature (K), (b) pH and initial concentration of dye (ppm), (c) pH and catalyst dosage (mg), (d) temperature (K) and initial dye concentration (ppm), (e) temperature (K) and catalyst dosage (mg), and (f) concentration of dye (ppm) and catalyst dosage (mg).

degradation rate of 96% was achieved at pH 8 and 328 K using a constant catalyst dose of 50 mg and an initial dye concentration of 10 ppm. Nevertheless, the anticipated deterioration could reach 99% at a temperature of 358 K. By observing the *F*-values of independent parameters (Table 4), the pH plays a main role in the degradation phenomenon, followed by the catalyst dosage, initial dye concentration and temperature. Moreover, pH change affects the surface charge of nanomaterials, ionic nature of dyes, adsorption capacity and band edge potentials. A low pH may result in the agglomeration of NPs if a charge is neutralized and a decrease in the adsorption of cationic dyes on NPs with a change in surface charge. After agglomeration, the surface area of NPs decreases and photocatalytic potential is alleviated. At pH above 9, the ionization of CMFE@NiO NPs starts due to hydrolysis, and Ni(OH)_2 becomes the predominant form, which again results in a decrease in NP concentration and reduced photocatalytic activity. Owing to the cationic nature of CV dye, the efficient adsorption of dye occurs at the surface of NPs at pH near 7, resulting in the best degradation efficiency. The catalytic efficiency is also reduced at a low pH due to the combination of H^+ ions with OH^- and $\cdot\text{OH}$ radicals. Hence, controlling pH is the main determining factor for the degradation of specific pollutants on the surface of nanomaterials.

After pH, catalyst dosage plays a major role in the degradation process, as evidenced by the *F*-value (Table 4). The degradation

efficiency increases with an increase in the active sites of NPs by increasing the catalyst dosage. However, at a very high catalyst dosage, the efficiency may decrease due to the agglomeration of particles by increased collisions and less penetration of light in suspension due to high turbidity. In the given range of parameters, it can be observed that the maximum degradation occurred at pH 8 and the highest catalyst dosage (~ 50 mg), as depicted in Fig. 6(c).

After catalyst dosage, the initial dye concentration affects the degradation efficiency and maximum %degradation can be observed at the lowest dye concentration at pH 8 and maximum catalyst dosage (50 mg), as shown in Fig. 6(b) and (f). As the concentration of dye increases, the competition between dye molecules increases to occupy the active sites of the catalyst. Owing to limited active sites, the %degradation is reduced at a given period of 120 minutes. Moreover, at very high concentrations of dye, the light penetration may reduce in the suspension, resulting in decreased %degradation.

Temperature played the minimum role in the %degradation of dye in the given range, as shown in Fig. 6(d) and (e). By increasing the temperature, the K.E. of dye molecules increases and the rate of degradation increases but up to a small extent, as evident from the *F*-value in the ANOVA analysis (Table 4).

The perturbation plot depicts the combined effect of all parameters/reaction conditions on the response at a particular



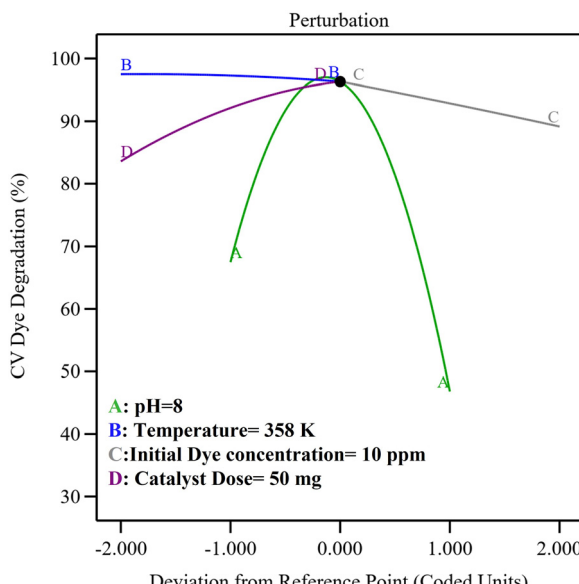


Fig. 7 Perturbation plot of variable effects on CV dye degradation (%).

point in the design space, as shown in Fig. 7. From the curvatures of factors, it can be clearly observed that the pH (A) and catalyst dose (D) are most influential in affecting the degradation phenomenon. The %degradation significantly varied as the pH and catalyst dose changed due to the change in surface charge on dye molecules and catalyst surface caused by a change in pH, variance of surface area and the number of active sites due to the change in the catalyst dosage. Moreover, under the optimized conditions of pH 8, temperature 358 K, initial dye concentration 10 ppm and catalyst dose of 50 mg, maximum degradation of dye was observed experimentally.

To evaluate the degradation kinetics, dye degradation (%) was calculated using eqn (5) every 15 min for 120 min under optimized conditions of pH 8, 50 mg catalyst dosage, and 10 ppm initial dye concentration at various temperatures, as shown in Fig. 8(a). The kinetics of degradation were studied by pseudo-1st order kinetics using eqn (10). The degradation data were well fitted into eqn (10) with R^2 values above 0.990 for CV

degradation, as shown in Fig. 8(b). The slope of this plot gives the k values of $2.07 \times 10^{-2} \text{ min}^{-1}$, $2.29 \times 10^{-2} \text{ min}^{-1}$, $2.78 \times 10^{-2} \text{ min}^{-1}$, $2.94 \times 10^{-2} \text{ min}^{-1}$ and $3.81 \times 10^{-2} \text{ min}^{-1}$ at 298 K, 313 K, 328 K, 343 K, and 358 K, respectively. It was observed that the rate of reaction increases with the increase in temperature, which illustrates the endothermic nature of the degradation reaction. These results demonstrate the promising potential of the synthesized NiO NPs as photocatalysts. This result was further supported by a comparison with the previously reported literature, as illustrated in Table S2 of the ESI.†

$$\ln \frac{C_0}{C_t} = kt \quad (10)$$

3.7. Effect of radical scavengers and proposed mechanism

Organic pollutants are rapidly degraded by ROS, including hydroxyl radicals, superoxide anion radicals, hydrogen peroxide, and holes. Batchwise radical scavenging tests assessed the production and major species involved using four scavengers: *p*-benzoquinone (*p*-BQ) for H_2O_2 scavenging, isopropyl alcohol (IPA) for OH^\bullet scavenging, disodium ethylenediamine tetraacetate (Na_2EDTA) for h^+ scavenging, and L-ascorbic acid (L-AA) for $\text{O}_2^{\bullet-}$ scavenging following the reported method.³⁶ In every run of the experiment, 50 mg of catalyst was added to a 10-ppm dye solution (20 mL), and 10 mL of a 0.2 mM solution of one radical scavenger was dissolved in it. The previously discussed method was used to monitor each dye's rate of degradation.

Fig. 9(a) shows the results of radical scavenging studies, which show that the presence of all radical scavengers reduces the dye degradation percentage. This indicates that all reactive species were formed in the solution when exposed to sunlight. The degradation process was most suppressed by Na_2EDTA addition, indicating that h^+ had an active involvement in the degradation phenomena because by scavenging h^+ , the %degradation significantly decreased. Further suppression of the degradation process was observed in the presence of IPA, which showed the active role of OH^\bullet after h^+ . Relatively low suppression of the degradation of CV in the presence of *p*-BQ and L-AA showed the least involvement of H_2O_2 and $\text{O}_2^{\bullet-}$ in the degradation process.

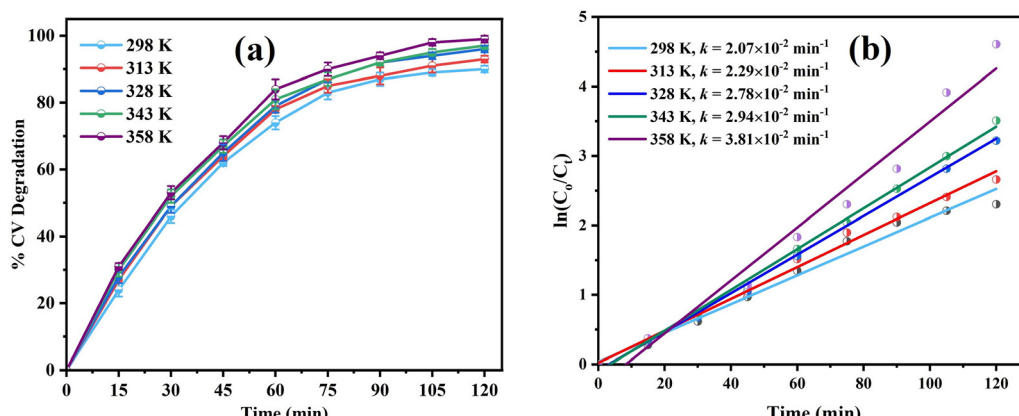


Fig. 8 (a) %Degradation of dyes vs. time. (b) Kinetics graph of degradation of CV dye.



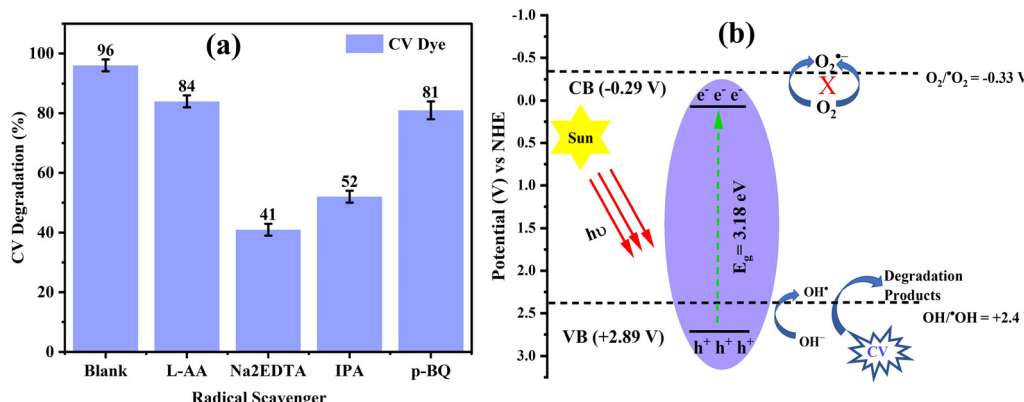


Fig. 9 (a) Effect of radical scavengers on the degradation of CV. (b) CV photodegradation mechanism of CMFE@NiO NPs, showing the position of VB and CB.

To correlate the experimental results with the band edge positions of VB and CB, the potentials of energy levels were estimated by Butler–Ginley equations (eqn (11) and (12)): ³⁷

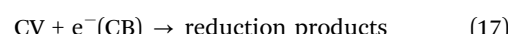
$$E_{CB} = X - E_C - 0.5E_g \quad (11)$$

$$E_{VB} = E_{CB} + E_g \quad (12)$$

where X , and E_C and E_g represent Mulliken's electronegativity and the energy of free electrons (4.5 eV). E_{CB} and E_{VB} were found to be -0.29 V and $+2.89$ V, respectively, as shown in Fig. 9(b). These values of E_{CB} and E_{VB} displayed the easy generation of reactive destructive species (h^+ and OH^\bullet) at the interface of the catalyst surface and aqueous media due to feasible oxidation potentials for the generation of OH^\bullet , as shown in Fig. 9(b). However, $O_2^\bullet-$ ions were not effectively produced due to the lower potential of CB to reduce oxygen molecules.

By analyzing the effect of these radical scavengers in the degradation process, the degradation mechanism of azo dyes was proposed, as shown in eqn (13)–(17). It was postulated that the valence electrons of the catalyst are excited to the conduction band in the presence of sunlight radiation, resulting in the production of e^- and h^+ pairs. The e^- are absorbed by the

dissolved oxygen, and the h^+ reacts with water to produce OH^\bullet radicals. Several secondary radicals are produced in the mixture by secondary reactions and actively participate in the degradation phenomenon.



3.8. TOC analysis

Estimation of total organic carbon content by TOC analysis is an important test to evaluate waste water quality at an industrial scale. This test is often used in advanced oxidation processes, such as photocatalysis, to determine the extent of the complete mineralization of pollutants at the catalyst surface. Only the fading of the color of the dye solution cannot justify the complete conversion of dye molecules to CO_2 and

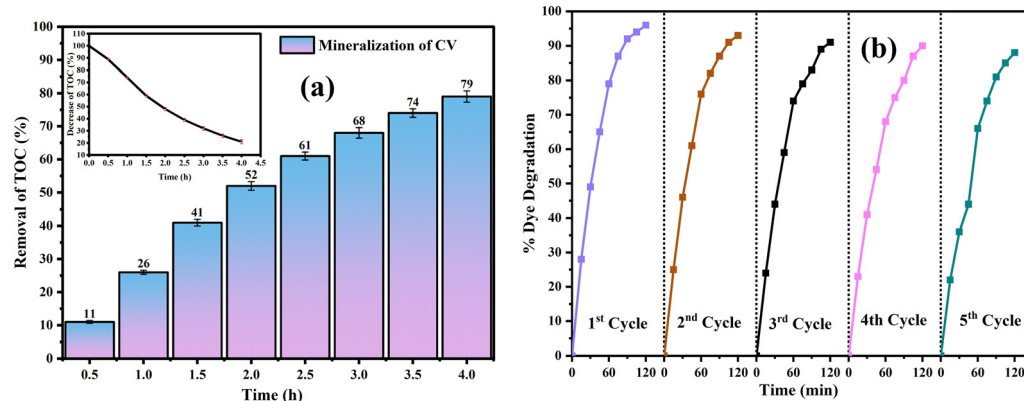


Fig. 10 (a) %Mineralization of CV dye after regular intervals of photodegradation. Inset is the decrease in TOC (%) over time. (b) Reusability results of CMFE@NiO NPs for the degradation of CV.



H_2O . The disappearance of color may be due to the breakdown of the chromophore group or the azo bond, which might have resulted in intermediate products. Therefore, TOC analysis is an important parameter for estimating the complete degradation of pollutants in water purification.³⁸ The process of dye mineralization was relatively sluggish in comparison to the disposal of color in the solution, as demonstrated by the calculation of TOC values at regular intervals (Fig. 10(a)). Measuring the TOC removal values after 4 h of sunshine exposure revealed that 79% of the CV dye was mineralized. Initially, the %removal of carbon content was slower due to the formation of reaction intermediates, but it gradually increased upon the complete degradation of organic carbon to CO_2 . The continuous decrease in TOC is also depicted in the inset of Fig. 10(a), which reaches 21% after 4 h. The gradual decomposition of stable nitrogen-containing species and many intermediates generated by photodegradation often cause mineralization to proceed at a slow rate.

3.9. Reusability studies of the photocatalyst

Using the previously described method,²⁵ the reusable nature of the photocatalyst was assessed for the degradation of CV dye for five consecutive cycles. In summary, the catalyst, *i.e.*, CMFE@NiO NPs, was recovered by centrifuging the mixture for 30 min at 3000 rpm. The solid catalyst was reused after rinsing three times with distilled water and drying for 4 h at 80 °C. The regeneration study's outcomes (Fig. 10(b)) demonstrated the catalyst's stability and capability for reuse with a minimal amount of activity alteration. After multiple usages, a mere 6% decrease in activity proved the catalyst's effectiveness for repeated usage. After appropriate activation, it seems that the described catalyst can be utilized several times for wastewater treatment. To examine the physical characteristics of regenerated CMFE@NiO NPs, the PXRD spectrum of the CMFE@NiO NPs was recorded in the 5th cycle. The PXRD spectrum indicated that the CMFE@NiO NPs remain stable and no significant change was observed. The PXRD spectrum of the used CMFE@NiO NP sample after the 5th cycle is presented in Fig. 11(a). All the characteristic peaks of NiO NPs were observed

in the PXRD spectrum with negligible shifting of the peaks, which demonstrated the high stability of NiO NPs after several uses. Similar results have been reported by some peers.³⁹ Similarly, the FTIR spectrum of CMFE@NiO NPs was also recorded after the 5th cycle. After the 5th cycle of regeneration (Fig. 11(b)), the FTIR spectrum of NPs indicated all the functional group peaks with a slight change in the peak positions. These results demonstrate the reusable nature of NiO NPs.

3.10. Biological activities of CMFE@NiO NPs

Pathogenic bacterial colonies in contaminated water bodies are the main cause of many water-borne diseases in animals and humans. Many microbes present in the discharges of hospitals, medical labs, and domestic and industrial wastes are directly mixed with the fresh water reservoirs prior to suitable disinfection in under developing countries. These bacteria may cause outbreaks of diseases such as diarrhea in Italy.⁴⁰ Some bacterial pathogens, their sources and possible infections are depicted in Table 5.

Among several disinfection methods, the production of ROS in water discharges by sunlight-activated nanocatalyst can be a viable approach. In this regard, many greenly synthesized nanomaterials are being evaluated for their antimicrobial potential to mitigate water pollution. Therefore, the antibacterial effectiveness of CMFE and CMFE@NiO NPs was evaluated against two Gram-positive strains (*S. aureus* and *B. subtilis*) and two Gram-negative strains (*E. coli* and *P. multocida*) using the disc diffusion method. As previously noted, CMFE is an effective bactericidal agent. An antibacterial assessment of the samples was conducted to test the synergistic impact of NPs combined with the capping of bioactive compounds. Efficiently encapsulating NPs with phytochemical species significantly boosts their antibacterial effectiveness *via* synergistic effects.¹³ Fig. 12(a) provides a comparison of the antibacterial activity of CMFE and CMFE@NiO NPs.

The results of the zone of inhibitions showed that compared to CMFE, the CMFE@NiO NPs were more effective and comparable to the broad spectrum standard drug, rifampicin (Fig. 12(a)). CMFE@NiO NPs showed good inhibition of all bacterial strains

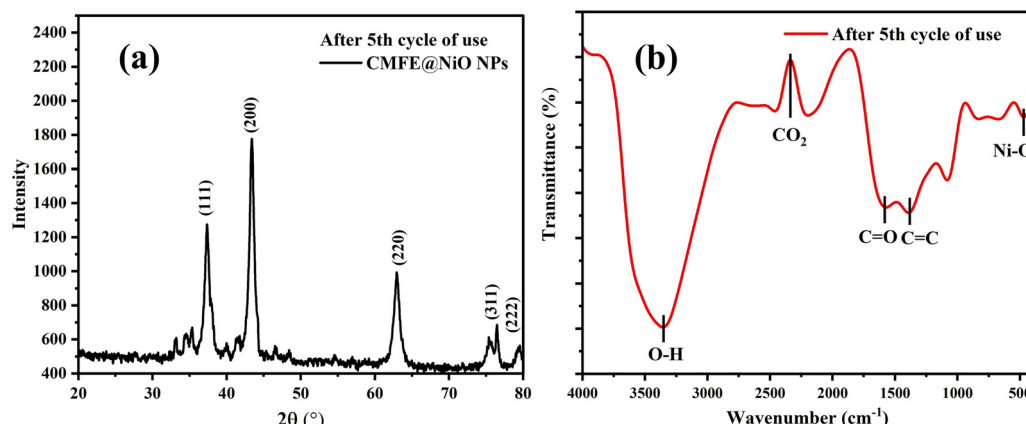


Fig. 11 (a) PXRD spectrum of CMFE@NiO NPs after the 5th cycle. (b) FTIR spectrum of CMFE@NiO NPs after the 5th cycle.



Table 5 Brief description of selective disease-causing pathogens

Pathogen	Strain	Infections/diseases caused by pathogen	Sources of pathogens in water bodies	Ref.
<i>E. coli</i>	Gram-negative	Enteritis, urinary tract infection (UTIs), septicemia and other clinical infections, such as neonatal meningitis, diarrhea	Hospitals, domestic waste, food industry waste and fecal pollution	41 and 42
<i>P. multocida</i>	Gram-negative	Respiratory infections, UTIs, skin infections, sepsis, soft tissue infections	Landfills, domestic waste, hospitals and medical labs	43 and 44
<i>S. aureus</i>	Gram-positive	Boils and abscesses, cellulitis, osteomyelitis, food poisoning, sepsis	Contaminated recreational waters and runoff from agricultural	45 and 46
<i>B. subtilis</i>	Gram-positive	Sepsis, bacteremia, skin and soft tissue infections	Hospitals and medical labs	47

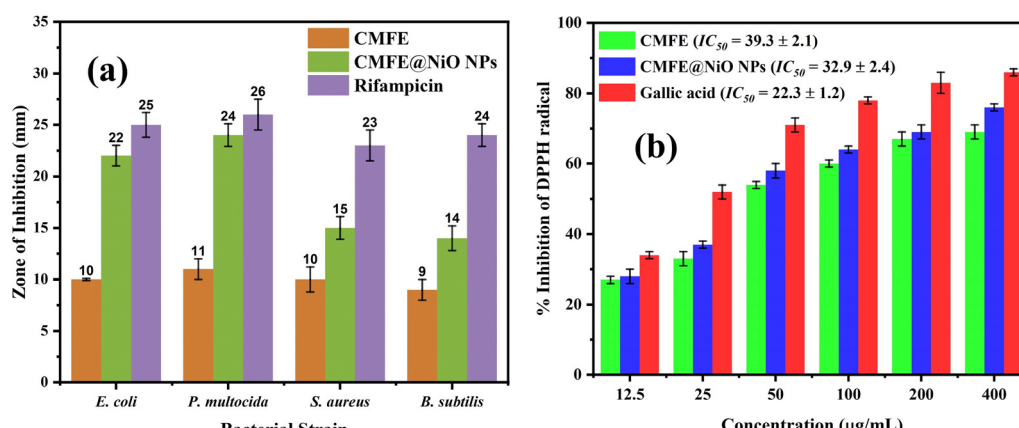


Fig. 12 (a) Inhibition zones obtained for different antibacterial strains by CMFE, CMFE@NiO NPs and rifampicin (positive control). (b) Antioxidant activity of CMFE, CMFE@NiO NPs and gallic acid (standard).

with inhibition diameters of 15 ± 1.5 mm, 14 ± 1.2 mm, 22 ± 2 mm and 24 ± 2.2 mm for *S. aureus*, *B. subtilis*, *E. coli* and *P. multocida*, respectively. Rifampicin showed inhibition diameters of 25 ± 1.2 mm, 26 ± 1.5 mm, 23 ± 1.5 mm and 24 ± 1.1 mm for *E. coli*, *P. multocida*, *S. aureus* and *B. subtilis*, respectively. The exact mechanism of action of NPs to hinder the growth of bacteria is still unknown. However, it has been previously demonstrated that ROS plays a major role by applying oxidative stress to bacterial membranes, resulting in the breakdown of membrane barriers and cell death.⁴⁸ Moreover, the generation of ROS within the cell, interaction of Ni^{2+} ions with

the membrane, and interaction of NPs with genetic material and growth protein inside the cell are also considered possible reasons for cell death if NPs gain access to the inside of the cell by crossing the membrane barriers. It is interesting to note that CMFE@NiO NPs caused greater deterioration of Gram-negative strains of bacteria. The remarkable activity of the CMFE@NiO NPs against Gram-negative bacteria was ascribed to the variations in the cell membranes of the bacterial strains. Gram-negative bacteria have very thin cell walls, making it easier for tiny particles to pass through and prevent the cell from normal functioning. Upon entering the cell, NiO NPs can easily interact

Table 6 Comparison of antioxidant activity of CMFE@NiO NPs with previously reported green synthesized NiO NPs

NPs	Extract	Assay	IC_{50} value ($\mu\text{g mL}^{-1}$)	Ref.
Ag	<i>Memecylon umbellatum</i>	DPPH	53.46	49
Ag	<i>Morus alba</i>	DPPH	97.27	50
		ABTS ^{•+}	25.92	
Au	<i>Lotus leguminosae</i>	DPPH	30.54	51
Au	<i>Plumbago zeylanica</i>	DPPH	68.53	52
Cu	<i>Falcaria vulgaris</i>	DPPH	190	53
CuO	<i>Cucurbita</i> sp.	DPPH	40.81	54
ZnO	<i>Knoxia sumatrensis</i>	DPPH	95.80	55
		ABTS ^{•+}	92.29	
NiO	<i>Ziziphus spina-christi</i> L.	H_2O_2	45.7	56
NiO	<i>Raphanus sativus</i>	ABTS ^{•+}	258	57
NiO	<i>C. macrocarpa</i>	DPPH	32.9 ± 2.4	Current work



with growth proteins, enzymes and DNA, ultimately resulting in cell death. There was a greater suppression of Gram-negative bacterial strains as a result of the enhanced entry of CMFE@NiO NPs within the cells and the combined action of NPs and capping agents.

The antioxidant activity of the samples and gallic acid as a standard was assessed by applying the DPPH radical scavenging assay. GA was used as a standard because it can easily scavenge and reduce the DPPH radical. The action of GA is associated with the existence of three hydroxyl groups that are known to have strong antioxidant properties. Furthermore, the detection of -OH peaks in the FTIR spectra of CMFE and CMFE@NiO NPs has attracted attention to investigate their antioxidant capabilities.

The DPPH assay results showed a dose-dependent increase in the DPPH radical scavenging potential of CMFE, CMFE@NiO NPs and gallic acid, as shown in Fig. 12(b). The NPs showed considerable antioxidant activity compared to the standard at high concentrations ($400 \mu\text{g mL}^{-1}$). This may be due to the capping of phytochemicals on the surface of the NiO NPs. The IC_{50} values have also shown a lower value of CMFE@NiO NPs ($32.9 \pm 2.4 \mu\text{g mL}^{-1}$) compared to the CMFE ($39.3 \pm 2.1 \mu\text{g mL}^{-1}$), which means the high activity of CMFE@NiO NPs than CMFE. Moreover, the CMFE@NiO NPs have shown a comparable IC_{50} to the gallic acid ($22.3 \pm 1.2 \mu\text{g mL}^{-1}$). As shown in Table 6, the comparison of CMFE@NiO NPs shows the highly efficient nature of these engineered biogenic NPs as an antioxidant agent, which has attracted further attention owing to their potential use in commercial products, such as creams and ointments.

4. Conclusion

Herein, green synthesis of CMFE@NiO NPs was reported using an aqueous extract of *C. macrocarpa* fruit. The UV-vis spectrum showed the SPR peak of the NiO NPs at 311 nm and a sunlight responsive bandgap of 3.18 eV calculated by Tauc plot. The presence of several functional group's peaks on the surface of the NPs confirmed the successful capping of bioactives on the surface of NPs. CMFE@NiO NPs with a crystallite size of 9.8 nm showed 99% degradation of CV under sunlight with a rate constant value of $3.81 \times 10^{-2} \text{ min}^{-1}$. The reaction conditions were optimized by applying the RSM/BBD model, which showed that maximum degradation was possible at pH 7 and a catalyst dose of 50 mg at 358 K in a 10 ppm dye solution. Radical scavenging experiments showed that holes, followed by OH^\bullet , were the main ROS involved in the degradation of CV. TOC analysis showed 79% mineralization of CV after 4 h exposure to sunlight. The antibacterial activity results showed that the CMFE@NiO NPs were more active against Gram-negative bacteria by inhibiting the growth of *E. coli* ($22 \pm 2 \text{ mm}$) and *P. multocida* ($24 \pm 2.2 \text{ mm}$) than the Gram-positive bacteria *S. aureus* ($15 \pm 1.5 \text{ mm}$) and *B. subtilis* ($14 \pm 1.2 \text{ mm}$), which might be due to the different cell wall structures of both strains. Antioxidant activity results showed a better reduction potential of

CMFE@NiO NPs ($\text{IC}_{50} = 32.9 \pm 2.4 \mu\text{g mL}^{-1}$) than extract ($\text{IC}_{50} = 39.3 \pm 2.1 \mu\text{g mL}^{-1}$). These experimental results demonstrated the commercial importance of these sunlight responsive greenly synthesized CMFE@NiO NPs for waste water purification of industrial effluents.

Author contributions

A. B. Siddique: methodology, investigation, writing – original draft, writing – review & editing. M. A. Shaheen: conceptualization, supervision, project administration, data curation. A. A. Abbas: conceptualization, writing – review & editing. Y. Zaman: project administration, resources. Shakra Shafeeq, Muhammad Zahid Ishaque & Muhammad Aslam: investigation & writing – review & editing. All authors reviewed and approved the manuscript.

Data availability

All evaluated data is available in the manuscript. Additional information/data can be provided upon reasonable request.

Conflicts of interest

The authors have no known financial or non-financial interests to disclose.

Acknowledgements

The authors declare that no funds, grants, or other support were received during the preparation of this manuscript.

References

- 1 S. H. Hashemi and M. Kaykhaii, *Emerging freshwater pollutants*, Elsevier, 2022, pp. 267–287.
- 2 P. Shandilya, P. Raizada and P. Singh, *Water Pollution and Remediation: Photocatalysis*, 2021, pp. 119–146.
- 3 W. Ahmad, S. C. Bhatt, M. Verma, V. Kumar and H. Kim, *Environ. Nanotechnol., Monit. Manage.*, 2022, **18**, 100674.
- 4 M. W. Alam, *Curr. Nanosci.*, 2021, **17**, 893–903.
- 5 Y. Gong, S. Zhang, H. Gao, Z. Ma, S. Hu and Z. A. Tan, *Sustainable Energy Fuels*, 2020, **4**, 4415–4458.
- 6 A. Singh, V. Goyal, J. Singh, H. Kaur, S. Kumar, K. M. Batoo, J. Gaur, M. Pal, M. Rawat and S. Hussain, *J. Cleaner Prod.*, 2022, **343**, 131026.
- 7 K. Kannan, D. Radhika, M. P. Nikolova, K. K. Sadasivuni, H. Mahdizadeh and U. Verma, *Inorg. Chem. Commun.*, 2020, **113**, 107755.
- 8 H. E. Khalil, Y. M. Aljeshi and F. A. Saleh, *J. Pharm. Sci. Res.*, 2015, **7**, 497.
- 9 F. Seke, V. E. Manhivi, T. Shoko, R. M. Slabbert, Y. Sultanbawa and D. Sivakumar, *Foods*, 2021, **10**, 1420.

10 F. Souilem, M. I. Dias, L. Barros, R. C. Calhelha, M. J. Alves, F. Harzallah-Skhiri and I. C. Ferreira, *Molecules*, 2019, **24**, 1696.

11 N. M. Mahmoodi, S. Keshavarzi and M. Ghezelbash, *J. Environ. Chem. Eng.*, 2017, **5**, 3684–3689.

12 D. Solomon, Z. Kiflie and S. Van Hulle, *Int. J. Ind. Chem.*, 2020, **11**, 43–53.

13 N. Al-Zaqri, K. Umamakeshvari, V. Mohana, A. Muthuvel and A. Boshala, *J. Mater. Sci.: Mater. Electron.*, 2022, **33**, 11864–11880.

14 B. Ahmad, M. Khan, M. Naeem, A. Alhodaib, M. Fatima, M. Amami, E. A. Al-Abbad, A. Kausar, N. Alwadai and A. Nazir, *Mater. Chem. Phys.*, 2022, **288**, 126363.

15 T. Riaz, A. Munawar, T. Shahzadi, M. Zaib, S. Shahid, M. Javed, S. Iqbal, K. Rizwan, M. Waqas and B. Khalid, *Inorg. Chem. Commun.*, 2022, **142**, 109656.

16 A. B. Siddique, M. A. Shaheen, A. Abbas, Y. Zaman, A. Ali, M. Naeem-ul-Hassan and J. Iqbal, *J. Environ. Chem. Eng.*, 2024, **12**, 112725.

17 S.-J. Hong, H.-J. Mun, B.-J. Kim and Y.-S. Kim, *Micromachines*, 2021, **12**, 1168.

18 A. B. Siddique, D. Amr, A. Abbas, L. Zohra, M. I. Irfan, A. Alhoshani, S. Ashraf and H. M. Amin, *Int. J. Biol. Macromol.*, 2024, **256**, 128009.

19 A. Ejaz, Z. Mamtaz, I. Yasmin, M. Shaban, A. B. Siddique, M. I. Irfan, A. Ali, S. Muhammad, M. Y. Sameeh and A. Abbas, *J. Mol. Liq.*, 2024, **393**, 123622.

20 Y. Zaman, M. Z. Ishaque, K. Waris, M. Shahzad, A. B. Siddique, M. I. Arshad, H. Zaman, H. M. Ali, F. Kanwal and M. Aslam, *Arabian J. Chem.*, 2023, **16**, 105230.

21 G. K. Weldegebreal, H. H. Dube and A. K. Sibhatu, *Int. J. Environ. Anal. Chem.*, 2023, **103**, 6146–6168.

22 I. K. Konstantinou and T. A. Albanis, *Appl. Catal., B*, 2004, **49**, 1–14.

23 W. W. Anku, S. O.-B. Oppong, S. K. Shukla and P. P. Govender, *Acta Chim. Slov.*, 2016, **63**, 380–391.

24 C. Lara-Pérez, E. Leyva, B. Zermeño, I. Osorio, C. Montalvo and E. Moctezuma, *Environ. Earth Sci.*, 2020, **79**, 277.

25 Y. Zaman, M. Z. Ishaque, Y. Yousaf, M. Shahzad, A. B. Siddique, M. I. Arshad, M. Sajid, N. Ali and G. Nabi, *Environ. Sci. Pollut. Res.*, 2023, **30**, 95860–95874.

26 M. Z. Ishaque, Y. Zaman, M. Shahzad, A. B. Siddique, S. Shahid, M. Akram, H. Kanwal, M. T. Akhtar and S. Hussain, *Water, Air, Soil Pollut.*, 2023, **234**, 252.

27 M. S. Ahmad, A. B. Siddique, M. Khalid, A. Ali, M. A. Shaheen, M. N. Tahir, M. Imran, A. Irfan, M. U. Khan and M. W. Paixão, *RSC Adv.*, 2023, **13**, 9222–9230.

28 F. Ascencio, A. Bobadilla and R. Escudero, *Appl. Phys. A: Mater. Sci. Process.*, 2019, **125**, 1–7.

29 P. K. Sharma, M. K. Singh, G. D. Sharma and A. Agrawal, *Mater. Today: Proc.*, 2021, **43**, 3061–3065.

30 N. M. Hosny, *Polyhedron*, 2011, **30**, 470–476.

31 M. Akram, A. H. Junaid, M. Z. Ishaque, Y. Zaman, M. Shahzad, A. B. Siddique, H. Kanwal, M. A. ur Rehman, M. I. Arshad and D. Ali, *Phys. Scr.*, 2024, **99**, 045938.

32 Y.-L. T. Ngo and S. H. Hur, *Mater. Res. Bull.*, 2016, **84**, 168–176.

33 M. W. Alam, *Appl. Organomet. Chem.*, 2024, e7899.

34 M. W. Alam, *Opt. Mater.*, 2024, **152**, 115401.

35 L. A. Sarabia and M. C. Ortiz, Response surface methodology, in *Comprehensive Chemometrics: Chemical and Biochemical Data Analysis*, ed. S. D. Brown, R. Tauler and B. Walczak, Elsevier B.V, The Netherlands, 2009, vol. 1, pp. 345–390.

36 D. T. C. Nguyen, H. T. Le, T. T. Nguyen, T. T. T. Nguyen, L. G. Bach, T. D. Nguyen and T. Van Tran, *J. Hazard. Mater.*, 2021, **420**, 126586.

37 M. A. Ashraf, C. Li, D. Zhang, L. Zhao and A. Fakhri, *Int. J. Biol. Macromol.*, 2021, **169**, 436–442.

38 M. Kus, S. Ribbens, V. Meynen and P. Cool, *Catalysts*, 2013, **3**, 74–87.

39 K. Hamidian, A. H. Rigi, A. Najafidoust, M. Sarani and A. Miri, *Bioprocess Biosyst. Eng.*, 2021, **44**, 2667–2678.

40 M. Escher, G. Scavia, S. Morabito, R. Tozzoli, A. Maugliani, S. Cantoni, S. Fracchia, A. Bettati, R. Casa and G. Gesu, *Epidemiol. Infect.*, 2014, **142**, 2559–2566.

41 N. Allocati, M. Masulli, M. F. Alexeyev and C. Di Ilio, *Int. J. Environ. Res. Public Health*, 2013, **10**, 6235–6254.

42 S. T. Odonkor and J. K. Ampofo, *Microbiol. Res.*, 2013, **4**, e2.

43 J. K. Miflin, X. Chen and P. J. Blackall, *Avian Pathol.*, 2000, **29**, 271–287.

44 J. Stec, U. Kosikowska, M. Mendrycka, D. Stępień-Pyśniak, P. Niedźwiedzka-Rystwej, D. Bębnowska, R. Hrynkiewicz, J. Ziętara-Wysocka and E. Grywalska, *Int. J. Environ. Res. Public Health*, 2022, **19**, 7308.

45 L. R. Plano, A. C. Garza, T. Shibata, S. M. Elmir, J. Kish, C. D. Sinigalliano, M. L. Gidley, G. Miller, K. Withum and L. E. Fleming, *BMC Microbiol.*, 2011, **11**, 1–10.

46 A. O. Oladipo, O. G. Oladipo and C. C. Bezuidenhout, *J. Water Health*, 2019, **17**, 930–943.

47 U. Anand, B. Reddy, V. K. Singh, A. K. Singh, K. K. Kesari, P. Tripathi, P. Kumar, V. Tripathi and J. Simal-Gandara, *Antibiotics*, 2021, **10**, 374.

48 N. Behera, M. Arakha, M. Priyadarshinee, B. S. Pattanayak, S. Soren, S. Jha and B. C. Mallick, *RSC Adv.*, 2019, **9**, 24888–24894.

49 M. S. AlSalhi, K. Elangovan, A. J. A. Ranjitsingh, P. Murali and S. Devanesan, *Saudi J. Biol. Sci.*, 2019, **26**, 970–978.

50 D. Das, R. Ghosh and P. Mandal, *SN Appl. Sci.*, 2019, **1**, 1–16.

51 M. H. Oueslati, L. B. Tahar and A. H. Harrath, *Arabian J. Chem.*, 2020, **13**, 3112–3122.

52 S. Priya Velammal, T. A. Devi and T. P. Amaladhas, *J. Nanostruct. Chem.*, 2016, **6**, 247–260.

53 M. M. Zangeneh, H. Ghaneialvar, M. Akbaribazm, M. Ghanimatdan, N. Abbasi, S. Goorani, E. Pirabbasi and A. Zangeneh, *J. Photochem. Photobiol., B*, 2019, **197**, 111556.

54 K. Velsankar, S. Sudhahar and G. Maheshwaran, *J. Photochem. Photobiol., B*, 2019, **200**, 111650.

55 S. Loganathan, M. S. Shivakumar, S. Karthi, S. S. Nathan and K. Selvam, *Toxicol. Rep.*, 2021, **8**, 64–72.

56 B. H. Shnawa, P. J. Jalil, S. M. Hamad and M. H. Ahmed, *Bionanoscience*, 2022, **12**, 1264–1278.

57 S. Haq, S. Dildar, M. B. Ali, A. Mezni, A. Hedfi, M. I. Shahzad, N. Shahzad and A. Shah, *Mater. Res. Express*, 2021, **8**, 055006.

